Experimental realization of an epsilon-near-zero graded-index metalens at terahertz frequencies

Victor Pacheco-Peña,[1,2] Nader Engheta,[2] Sergei Kuznetsov,[3-5] Alexandr Gentselev,[4] Miguel Beruete,[1,6*]

[1]Antennas Group-TERALAB, Universidad Pública de Navarra, Campus Arrosadía, 31006 Pamplona, Spain
[2]Department of Electrical and Systems Engineering, University of Pennsylvania, Philadelphia, PA 19104, USA
[3]Novosibirsk State University, Pirogova Str. 2, 630090 Novosibirsk, Russian Federation
[4]Budker Institute of Nuclear Physics SB RAS, Lavrentiev Ave. 11, 630090 Novosibirsk, Russian Federation
[5]Institute of Semiconductor Physics SB RAS, Novosibirsk Branch "TDIAM", Lavrentiev Ave. 2/1, Novosibirsk, 630090, Russian Federation
[6]Institute of Smart Cities, Public University of Navarra, 31006 Pamplona, Spain

*Corresponding author: miguel.beruete@unavarra.es

The THz band has been historically hindered by the lack of efficient generators and detectors, but a series of recent breakthroughs have helped to effectively close the "THz gap". A rapid development of THz technology has been possible thanks to the translation of revolutionary concepts from other regions of the electromagnetic spectrum. Among them, metamaterials stand out for their unprecedented ability to control wave propagation and manipulate electromagnetic response of matter. They have become a workhorse in the development of terahertz (THz) devices such as lenses, polarizers, etc. with fascinating features. In particular epsilon-near-zero (ENZ) metamaterials have attracted much attention in the past several years due to their unusual properties such as squeezing, tunneling and supercoupling where a wave traveling inside of an electrically small channel filled with an ENZ medium can be tunneled through it reducing reflections and coupling most of its energy. Here, we design and experimentally demonstrate an ENZ graded-index (GRIN) metamaterial lens operating at THz with a power enhancement of 16.2 dB, using an array of narrow hollow rectangular waveguides working near their cut-off frequencies. This is the first demonstration of an ENZ-GRIN device at THz and can open the path towards other realizations of similar devices enabling full quasi-optical processing of THz signals.

PACS: 52.40.Fd, 42.82.Et, 41.20.Jb, 78.66.Sq

I.   Introduction

Metamaterials have demonstrated to allow a successful control of the electromagnetic response of media opening the gate to manipulation of wave propagation [1–14]. Within this realm, metamaterials with a relative permittivity near zero (known as epsilon near-zero (ENZ)) exhibit fascinating features that have been recently studied in different frequency bands of the electromagnetic spectrum, mainly microwaves, millimeter-waves, near infrared and optical frequencies [15–29]. Much of the attention is due to the fact that the waves traveling inside these media show almost "infinite" phase velocity and wavelength, with nearly uniform spatial phase variation, giving rise to unconventional phenomena such as tunneling, squeezing and supercoupling [16]. It has been demonstrated that a simple and efficient way to emulate the response of a ENZ metamaterial is to utilize narrow hollow rectangular metallic waveguides working near their cut-off frequencies [26]. This configuration has been proposed in the design of sensors [30], control of tunneling with nonlinearities [31], beamshaping [32–36], enhanced molecular fluorescence [37] and impedance matched devices [38]. Lenses have also benefited greatly from ENZ metamaterials [33,36] as they offer the possibility to tailor arbitrarily the wave front at the output by simply shaping the interface profile. As demonstrated in [33], a focus can be generated at any desired position by simply profiling the output face of a uniform ENZ lens with a concave shape. The main drawback of such structures is their bulkiness due to their profiled faces. To overcome this limitation without deteriorating their performance, ENZ-graded-index (ENZ-GRIN) devices have been theoretically proposed in previous works [34,35].

Even though ENZ metamaterials have been demonstrated over several spectral regimes [20,21,23,26,39], the application of these concepts to the THz frequency band (0.1-10 THz) has been a major challenge due to the lack of appropriate fabrication and testing technologies in this band. Typical fabrication constraints at THz imposed on the structure thickness relevant for ENZ-GRIN implementation are of the order of hundreds of microns, whereas the lateral dimensions of the structure are to be maintained at micrometer accuracy. Such a thickness is too small for conventional microwave techniques and too large for standard optical lithography. In fact, this is another important reason that has hampered the development of THz technologies, contributing to the famous "THz-gap" [40–45]. Even though there is still a need for several technological improvements to be fulfilled, a great progress has been achieved in this frequency range, to the extent that modulators [43], multiplexers [46] and tunable devices [47,48] have been

recently demonstrated. At the same time as the gap is getting "closed", a growing interest in the design of metamaterials at THz frequencies arises [41] and different metadevices have been recently proposed [42,49–51] demonstrating that the design of metamaterial-based devices within this frequency range is no longer elusive.

Inspired by the exciting features of ENZ metamaterials and the importance of the THz frequency band, here we present the first experimental demonstration of an ENZ-GRIN lens operating at THz frequencies. The structure is designed based on the recently proposed lens reported in ref. 34 using an array of narrow hollow rectangular waveguides working near their cut-off frequencies, thus emulating an ENZ metamaterial (Fig. 1). It is designed to work at 0.706 THz (λ = 0.428 mm) transforming an incident plane wave into a narrow focus situated at 6 mm (14λ) from the output of the lens.

II. Results

a. Design of the ENZ-GRIN lens

The basic principle to emulate an effective ENZ medium using a rectangular waveguide [see Fig. 1(b)] relies on its intrinsic structural dispersion. By restricting the problem to monomode TE_{01} operation (only the fundamental TE_{01} mode of propagation) the dispersion relation of the waveguide can be written as [26,52]:

$$\beta = k_0 \sqrt{\mu_{reff}\, \varepsilon_{reff}} = k_0 \sqrt{1 - \left(\frac{\pi}{k_0 h_y}\right)^2} = k_0 \sqrt{1 - \left(\frac{f_c}{f}\right)^2}$$

(1)

Here, it has been assumed that the waveguide behaves as an equivalent medium with an effective permittivity and permeability, (μ_{reff}, ε_{reff}), $k_0 = 2\pi/\lambda_0$ is the wavenumber at the free-space wavelength λ_0, h_y is the larger hollow dimension of the waveguide, f_c is the cut-off frequency of the fundamental TE_{01} mode and f is the operating frequency. For this mode, $\mu_{reff} = 1$ [26]. Thus, the waveguide is equivalent to an effective medium with a dispersive relative effective permittivity that can be evaluated from Eq. (1). As can be seen from this equation, near the cut-off frequency of this mode ε_{reff} is close to zero, which means that the waveguide emulates an effective ENZ medium. This performance can be observed in Fig. 1(b) where the spectral response of the waveguide is evaluated in terms of the ε_{reff} and Re$\{\beta/k_0\}$. As it is shown, near cut-off the ENZ condition is achieved with Re$\{\beta/k_0\} \approx 0$. This principle is applied here

to the design of our ENZ-GRIN metamaterial lens by constructing a matrix of waveguides whose dimensions are gradually varied, as detailed below.

With the GRIN technique, each waveguide of the array must introduce a prescribed phase delay ($\Delta\Phi$) to generate a focus at the desired distance. This phase delay can be calculated by ray tracing, assuming that the lens is discretized along both x and y axes, and can thus be expressed as:

$$\Delta\Phi^{(m,n)} = \beta^{(0,0)}l_z - k_0\left[\sqrt{FL^2 + \left(md_x\right)^2 + \left(nd_y\right)^2} - FL\right] + 2\pi\alpha.$$

(2)

where m and n are integers and define the discretization (i.e., each waveguide) of the array along the x and y axes, $\beta^{(0,0)}$ is the propagation constant of the waveguide at the center of the array (reference waveguide, see dimensions in Fig. 1(b)), l_z is the thickness of the lens, FL is the focal length, d_x and d_y are the periods along x and y and α is an integer number ($\alpha = 1,2,3\ldots$). As deduced from the above equation, the phase delay introduced by each waveguide must balance the phase difference between the output of the lens and the focus.

The larger dimension of the reference waveguide is designed to fix the cut-off at 0.7 THz ($h_y = \lambda_0/2$). Nevertheless, it has been demonstrated in previous works [30,33,34,53] that the ENZ condition happens close to, but not exactly at the cut-off frequency due to the finite size of the waveguide along the z axis. Using a numerical simulation of the central waveguide and applying the local periodicity approximation [34,35], it was found that ENZ operation occurs at 0.706 THz. Hereafter, we take this as the design frequency of the lens, although we anticipate a slight deviation from this value due to the error introduced by the local periodicity approximation (obviously, the GRIN condition implies that each waveguide of the array must have different hollow dimensions).

Under the ENZ approximation the dimension $h_y^{(m,n)}$ controls the required phase delay, as determined from Eqs. (1-2). The short side $h_x^{(m,n)}$ provides impedance matching with free space if it is made sufficiently narrow [34,35]. The equation that governs this dimension assuming $\mu_{reff} = 1$ is [16,18]:

$$h_x^{(m,n)} = \frac{\beta^{(m,n)}h_y^{(m,n)}d_x}{k_0 d_y}.$$

(3)

As mentioned before, Eqs. (1,3) are valid when working close to the cut-off frequency of the

fundamental TE_{01} (monomode). If the design frequency were selected to be far from cut-off, Eqs. (1,3) would not be longer valid. Hence, in order to avoid undesirable responses because of a multimodal performance and to be able to engineer both the $h_y^{(m,,n)}$ and $h_x^{(m,,n)}$ dimensions, the ENZ region is needed. With these conditions, the ENZ-GRIN metamaterial lens can be designed, see schematic in Fig. 1(a). It consists of 11817 narrow hollow rectangular waveguides (101 × 117 waveguides along the x and y axes, respectively) with a total physical size of 54.1 mm × 50.14 mm × 1 mm ($x \times y \times z$). The hollow dimensions of each waveguide are obtained from Eqs. (1-3), with more details provided in the Appendix section 1 (Fig. 5). In Fig. 1(c) the values of the relative effective permittivity (ε_{reff}) of each waveguide retrieved from Eq. (1) are presented. Additionally, we have extracted the values for the two principal axes x and y and have plotted them in Fig. 1(d-e). From these figures one can observe that all waveguides work properly within the ENZ approximation, with $\varepsilon_{reff} < 0.25$ in all of them. The minimum permittivity value appears for the central waveguide ($\varepsilon_{reff} \sim 0.017$), as imposed by design. It is important to note that the ENZ-GRIN metalens designed here may bring to mind classical metallic lenses [54–56]. The main difference is that classical metallic lenses suffer from Fresnel reflections which are intrinsically present because of the impedance mismatch between the metallic waveguides and free-space. Similarly, common THz lenses are made of conventional dielectrics such as Teflon or Silicon. However, their main drawback are their increased thickness and high impedance mismatch, respectively [56,57]. To minimize losses produced by the impedance mismatch it is possible to apply different techniques such as using anti-reflection coatings or by properly engineering transmit-arrays or metasurface-based lenses[58,59]. As reported in [34] and shown in Eq. (3), the ENZ-GRIN metalens designed here minimizes this problem by modulating one hollow dimension for each waveguide of the array. The present work then corresponds to the experimental proof-of-concept of the proposed design and more details about numerical simulations can be found in [34].

b. **Experimental and numerical demonstration**

To demonstrate experimentally the performance of the ENZ-GRIN lens, a patented fabrication method based on a deep X-ray lithography (DXRL) technique [60,61] is employed in this work for manufacturing the lens prototype. The necessity of using DXRL is explained by a relatively high aspect ratio and actual thickness of the designed structure whose production is unattainable with optical lithography. In the proposed fabrication method, high-energy X-rays with a typical wavelength of 1 Å

generated by a synchrotron radiation source are used for the lithographic patterning of a polymethyl methacrylate (PMMA) layer followed by its entire surface metallization (see Fig. 6 and Fig. 7 of the Appendix section 2 for more details of the fabrication techniques). The PMMA layer has the thickness of the designed ENZ-GRIN lens (1 mm) and plays the role of carrying polymeric substrate, while the metallized (Ag/Al) layer deposited on the PMMA surface and having the typical thickness (~1 um) larger than the THz radiation skin depth allows the structure to act as fully metallic in terms of its electromagnetic response. The structures of this kind are referred to in literature as "pseudo-metallic" [60,61]. It is worth noting that their fabrication is much simpler and less expensive in comparison with a conventional LIGA technology [62], which is normally used for producing high-aspect-ratio entirely metallic structures (with no dielectric core inside). Figure 2(a) illustrates the fabricated lens mounted on a circular holder with a clear aperture diameter of 50 mm. A microscope photograph and a picture taken from the numerical simulator showing nine waveguides at the center of the structure are shown in Fig. 2(b) and Fig. 2(c), respectively. From these figures we can estimate that the fabrication is sufficiently accurate even taking into account the stringent aspect ratio of the waveguides: the narrow hollow dimension is of the order of just a few tens of microns whereas the depth of the waveguides is 1 mm. For the sake of completeness, a more general view of the fabricated ENZ-GRIN lens along with a schematic representation showing more waveguides are shown in Fig. 2(d-e), comparing the design with the fabricated prototype.

The lens is experimentally characterized with an ABmm[TM] Vector Network Analyzer. First, its broadband response is evaluated by measuring the power distribution along the lens axis (z axis) from 0.630 THz to 0.730 THz. The lens is placed between a diagonal horn antenna (used as a source) with the electric field polarized along the x direction (E_x) and a flange-ended rectangular waveguide (used as a receiver). By shifting the receiver along the z axis with micrometric precision, we measure the power distribution along the propagation direction. A full description of the setup is given in Fig. 8 in the Appendix section 3.

The experimental results are shown in Fig. 3(a). They are compared with numerical simulations performed with the commercial simulator CST Microwave Studio®, see Fig. 3(b) (for a description of the numerical setup see Appendix section 4). In general, a good agreement is found between numerical and experimental results: in the experiment the focus appears at (f, FL) = (0.675 THz, 6 mm) whereas in the simulation it is at (f, FL) = (0.692 THz, 6.25 mm). Recall that in the design we imposed (f, FL) =

(0.706 THz, 6 mm). Therefore aside from a small frequency shift, the lens has an excellent performance. As mentioned earlier, the error is probably due to the local periodicity approximation, which does not totally hold in our ENZ-GRIN prototype. Moreover, there are imperfections in the fabrication that might slightly alter the performance, such as waveguide cross sections being not completely rectangular and slight deviations of the hollow dimensions from the nominal values. In any case, the frequency error is very small ~1.89% in the simulation and ~4.36% in the experiment, especially taking into account that the fabrication of this lens is highly challenging.

In Fig. 3(c) we have plotted the power distribution along the z axis at the maximum frequency. From these curves we can extract the depth of focus (*DF,* defined as the distance at which the power distribution has decayed half of its maximum along the propagation direction) which is another important parameter in a lens performance. Again, we notice a good agreement between experimental results, *DF* $= 2.14\lambda_{exp}$ (0.95mm), and simulation results, $DF = 2.33\lambda_{sim}$ (1.01mm).

For a complete characterization, the power distribution at the focal point for both principal planes (E- and H- plane) is measured, see Appendix section 4 for a detailed information about the setup. The experimental results [Fig. 4(a,d)] are similar to the numerical simulations [Fig. 4(b,e)]. From these results, we observe clearly how the ENZ-GRIN lens can actually focus the incident wave onto a focal spot. It produces a high power enhancement at the *FL* of 42 times (16.23 dB) in the experiment (69 times (18.42 dB) in the simulation) compared to the value without lens. The small difference between simulation and measurement can be attributed to imperfections in fabrication such as metal roughness, waveguide dimensions, etc.

Finally, the power distribution at the focal plane along the x and y axis is plotted in Fig. 4(c,f) . Both experimental and simulation results present similar focus profiles, from which we can obtain the Full-Width at Half-Maximum (FWHM) (defined as the distance along the x or y axis at which the power has decayed half of its maximum). From the experimental results we get $FWHM_x = 0.217 \pm 0.01$ mm $=$ $(0.488 \pm 0.025)\lambda_{exp}$ and $FWHM_y = 0.337 \pm 0.01$ mm $= (0.76 \pm 0.025)\lambda_{exp}$ (in the simulation these values are $FWHM_x$ 0.238 mm $= 0.55\lambda_{sim}$ and $FWHM_y = 0.337$ mm $= 0.78\lambda_{sim}$).

III.   Conclusions

To sum up, we have demonstrated the first experimental realization of an ENZ-GRIN lens at THz

frequencies. The lens is based on a non-uniform array of narrow hollow rectangular metallic waveguides. A high power enhancement of 42 times of the incident power at the focal has been experimentally achieved at the frequency of 0.675 THz. The experimental values are in excellent agreement with the numerical simulations of the 3D lens. The results presented here may open doors to future work in this exciting frequency range, and may lead to other THz devices based on ENZ media such as beam steerers, sensors or beamshapers.
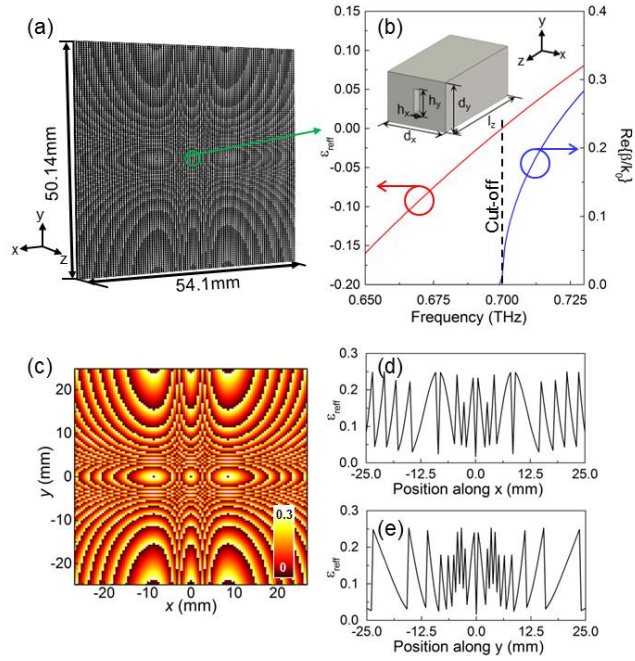
ACKNOWLEDGMENTS

Figure 1. (a) Schematic representation of the designed lens (artist rendition). (b) Artist presentation of the unit cell used as a central waveguide of the lens array along with the dispersive performance and ε_{reff} extracted from Eqs. (1). The waveguide has lateral periodicity of $d_x = 537.5$ μm and $d_y = 428.6$ μm, hollow dimensions of $h_x = 53.57$ μm, $h_y = 214.28$ μm and a lens thickness of $l_z = 1000$ μm. Effective permittivity of the designed ENZ-GRIN metamaterial lens: (c) complete lens, (d) along the x axis at $y = 0$ and (e) along the y axis at $x = 0$.
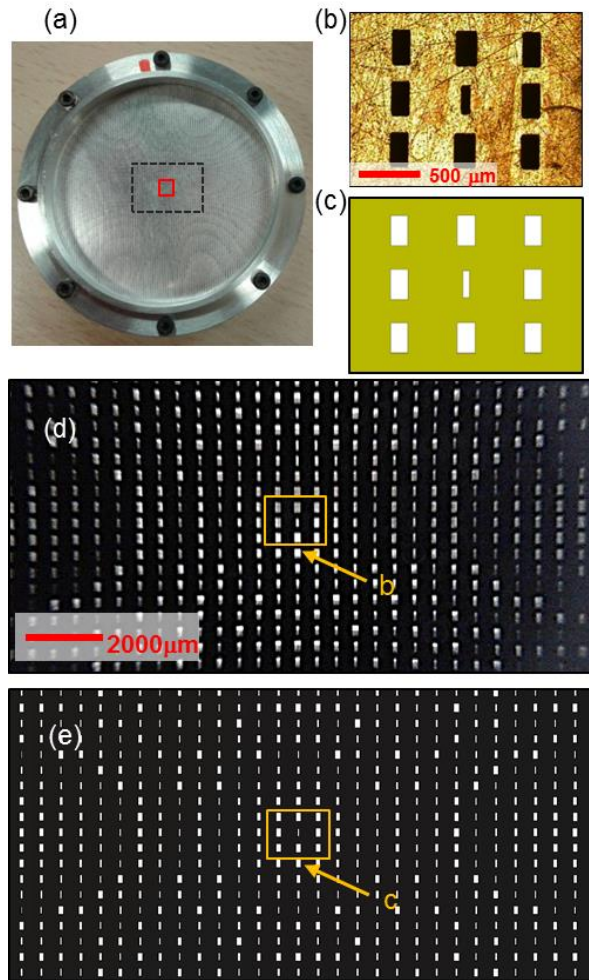
Figure 2. (a) Full photograph of the fabricated prototype (the black-dashed and red lines correspond to the zoom-in pictures shown in panels (d) and (b), respectively. (b), Zoom-in photograph of the nine central waveguides. (c) Schematic representation of the nine central waveguides taken from CST Microwave Studio®. (d) Picture of the fabricated prototype showing several waveguides. (e) Schematic representation of the simulated ENZ-GRIN metamaterial lens showing several waveguides (taken from CST Microwave Studio®).
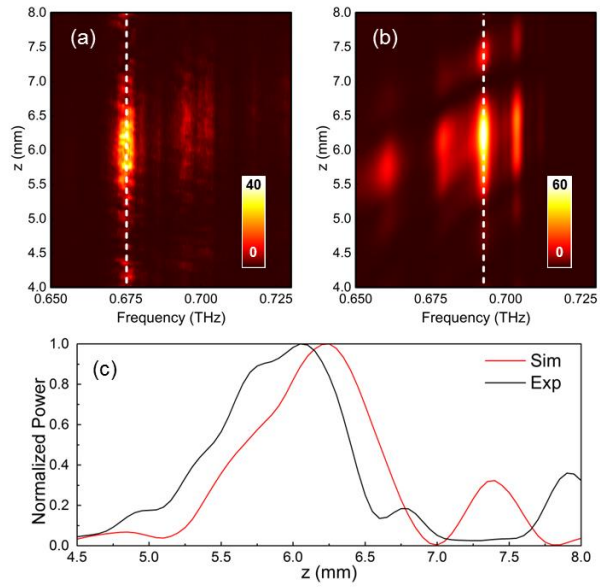
Figure 3. Power distribution along the propagation axis of the ENZ-GRIN lens vs frequency: (a) experimental and (b) numerical results. (c), Experimental (black line) and simulation (red line) results of the power distribution along the *z* axis at the frequency of maximum focus intensity, 0.675 THz (experiment) and 0.692 THz (simulation). The curves in (c) are extracted from the white dashed lines in panels (a) and (b) and are normalized to the maximum of each case to better compare them.
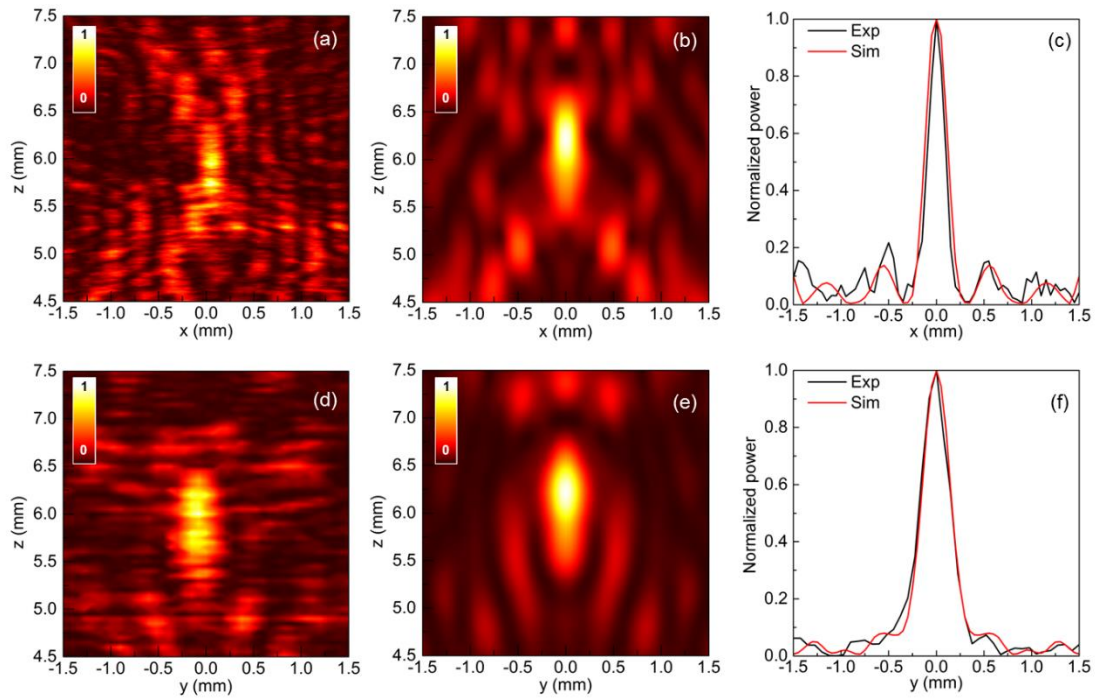
Figure 4. Experimental and numerical results for power distribution on the focal planes: (a) and (d) experimental results on the *xz* and *yz* planes, respectively, at *f* = 0.675 THz. (b) and (e) numerical results on the *xz* and *yz* planes, respectively, at *f* = 0.692 THz where the maximum fields are obtained. This frequency is slightly different from the one in the experiment due to fabrication imperfections. In the Appendix section 5, we also present the numerical results for *f* = 0.675 THz. (c) and (f) experimental (black lines) and numerical (red lines) results of the power distribution at the focal position along the *x* and *y* axes, respectively.

APPENDIX

1. Hollow dimensions

The hollow dimensions of the designed ENZ-GRIN metalens are shown in Fig. 5. The dimensions along the y (h_y) and x (h_y) for all the waveguides of the array are calculated using Eqs. (1,3) and are shown in panels (a) and (b), respectively. Also, the hollow dimensions along the x axis at $y = 0$ (white dashed lines of panels (a) and (b)) are shown in Fig. 5 (d) to better appreciate these results. As explained in the manuscript, each waveguide of the array should introduce a phase delay in order to produce a focus at the output of the lens. This phase delay has been controlled by changing the hollow dimension h_y. For the sake of completeness, the cut-off frequency of the fundamental mode for each waveguide is shown in Fig. 5 (c) calculated using Eq. 1. To better visualize these results, the cut-off frequency along the x axis at $y = 0$ are shown in Fig. 5 (e).
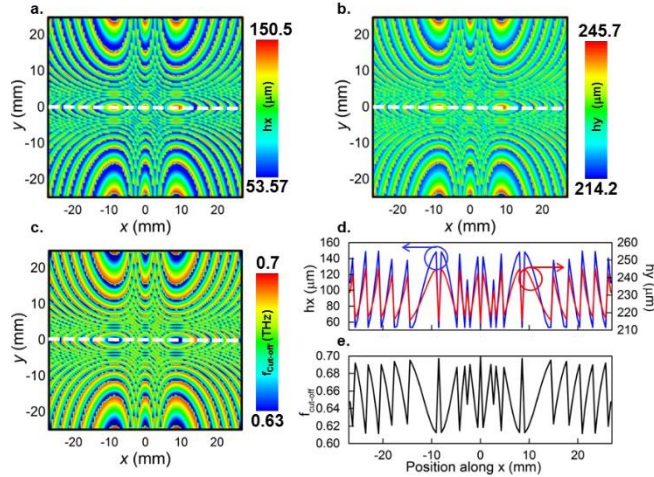

Figure. 5. Hollow dimensions of the designed ENZ-GRIN lens: (a) contour plot showing the value of h_x as a function of the waveguide position (x,y). (b) Idem for h_y. (c) Cut-off frequency of the fundamental mode for all the waveguides. Hollow dimensions (d) and cut-of frequency for the waveguides located along the x axis at $y = 0$. These values are obtained from the white dashed line of panels (a-c).

2. Fabrication techniques

The ENZ-GRIN lens prototype was manufactured using technological facilities of the Siberian Synchrotron and Terahertz Radiation Center (SSTRC, BINP SB RAS, Novosibirsk, Russia). The fabrication method is based on a deep X-ray lithography (DXRL) technique and implies the use of high-energy X-rays produced by a synchrotron radiation source at the VEPP-3 storage ring for radiation treatment. The X-rays spectrum of the source is concentrated near the wavelength of 1 Å that allows such "hard" radiation penetrating deeply into thick layers of X-ray-sensitive resists. Using an X-ray-contrast mask (X-mask) this enables forming patterned high-aspect microstructures having through-

holes with vertical walls.

The three basic stages of the fabrication process are shown in Fig. 6. First, the polished PMMA [$\varepsilon_{PMMA} \approx 2.58$ (1- $j5\times10^{-2}$)] layer 1 ± 0.01 mm thick, which serves both as the X-ray-sensitive and the lens-core material, is exposed to X-rays through the X-mask (a). The X-mask replicates the geometry of the designed ENZ-GRIN lens and is made as a patterned brass foil with the thickness $\Delta = 50 \pm 1$ um produced in advance via laser micromachining. At the second stage, due to radiation damage of molecular chains in PMMA upon its X-ray treatment, the irradiated parts of the PMMA layer are removed by chemical development (b). Finally, the entire surface of the patterned polymeric structure including inner walls of the waveguide holes is metallized via chemical deposition of a silver layer 0.1 um thick, which is further "enhanced" through magnetron sputtering of additional silver and aluminum layers with the total thickness of 1 um to form the highly conductive corrosion-resistant metallic coating (c).
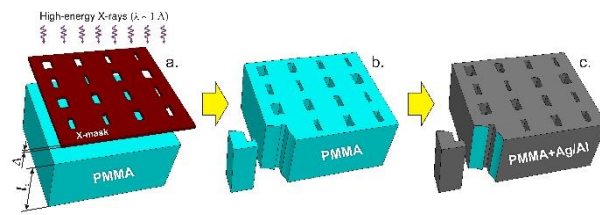

Figure. 6. Basic fabrication stages for the ENZ-GRIN lens: (a) irradiation of the PMMA layer by "hard" X-rays through the X-ray mask. (b) Chemical development of the patterned polymeric structure. (c) Metallization of the entire dielectric surface via depositing thin Ag/Al layers. The structural slice is introduced in (b and c) to show that PMMA is patterned through and all the waveguide holes have vertical walls.

Note that in the described fabrication technology the quality of the X-mask pattern is estimated to be the main factor limiting the ENZ-GRIN lens performance. Herein, we employed a homemade laser micromachining system based on a 10-ns-pulse Nd:YAG laser (λ_0=1064 nm, 10 kHz, 10 W) providing the diameter of 10 um for the laser beam focused onto the brass foil. The system exhibited the typical accuracy of ±3-5 um for irregularity of the hole's edge upon laser cutting, though somewhat larger geometrical deviations were tracked in fabrication (Fig. 7). It is noteworthy that such deviations do not cause a noticeable degradation of the ENZ-GRIN lens performance, as described in the manuscript.
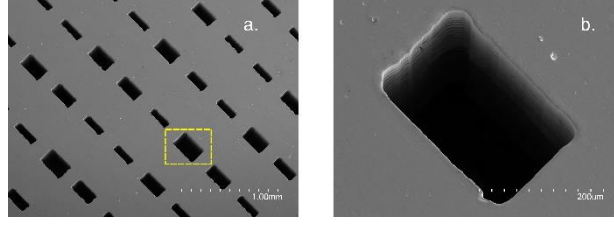
Figure. 7. SEM images of the fabricated ENZ-GRIN lens structure: (a) smaller scale. (b) larger scale. The geometry of the waveguide holes slightly deviates from the ideal rectangular geometry of the designed holes that originates from some imperfection of the X-ray mask upon its fabrication by laser micromachining.
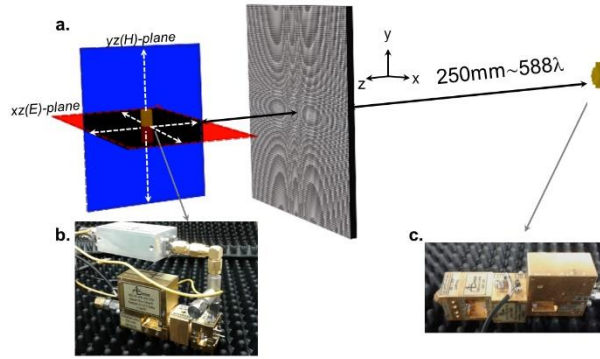
3. Experimental setup

Figure. 8. Schematic representation of the setup used to characterize experimentally the performance of the ENZ-GRIN lens: (a) Artist figure showing the lens placed in the middle of a diagonal horn antenna (source) and a flange ended waveguide (receiver). The latter was placed on a translational platform in order to record the power distribution on the focal planes along the *x, y* and *z* axes from 0.630THz to 0.730THz. (b) Photograph of the receiver. (c) Photograph of the transmitter.

The experimental measurements were carried out using an AB Millimetre$^{\text{TM}}$ quasi-optical vector network analyzer (VNA). A general sketch of the experimental setup is shown in Fig. 8. The ENZ-GRIN lens was placed in front of a standard diagonal horn antenna (WR-1.2) at 250 mm (~588λ at the design frequency of 0.706 THz). On the opposite side, a flange-ended rectangular waveguide (WR-1.2) was used as a receiver. It was placed on a translation stage in order to scan the power distribution near the focal plane. To characterize the broadband response of the lens shown in Fig. 3(a), the receiver was placed just at $x = y = 0$ and was moved along z from 4 mm to 8 mm with a very fine step of 0.05 mm (~0.117λ at the design frequency). With this configuration, the power distribution at each position was measured from 0.630 THz to 0.730 THz with a high resolution step of 0.0002 THz (200 MHz). For the focal planes shown in Fig. 4(a,d), the receiver was moved on the xz and yz planes in order to experimentally characterize the focusing properties of the lens on the *E* and *H* planes, respectively. A

high resolution measurement was performed by moving the receiver from -1.5 mm to 1.5 mm with a step of 0.01 mm (0.024λ) along the x/y axes and from 4.5 mm to 7.5 mm along the z axis with a step 0.05 mm (0.117λ).

4.   Numerical evaluation of the ENZ-GRIN metalens

The numerical analysis of the ENZ-GRIN lens was performed using the transient solver of the commercial software CST Microwave Studio®. For all the simulations, the full ENZ-GRIN lens was simulated. A horizontally polarized plane wave (E_x) was used to illuminate the lens from its back using Open+Add Space (i.e. perfectly matched layers) boundary conditions in all planes. Electric and magnetic symmetry planes were defined in the yz and xz planes, respectively, in order to reduce the simulation burden. Aluminum was used as the material of the lens with a conductivity of $\sigma = 3.56\times10^7$ S/m. A very fine meshing was used with a minimum and maximum mesh size of 0.0205 mm and 0.101 mm, respectively. With this configuration, the lens was simulated using a total number of ~82 million of cells. To characterize the broadband response of the lens, as shown in Fig. 3(b) of the manuscript, electric and magnetic probes were placed along the z axis (at $x = y = 0$) to record the field distributions at the same positions as in the experiment. Likewise, the frequency response was obtained in each position with the same spectral range and steps used in experiments. Finally, the broadband power distribution was calculated using the x and y components of the steady-state electric and magnetic field components, respectively, as ½($|E_x||H_y|$). After evaluating the broadband response, a second simulation of the ENZ-GRIN lens was performed to calculate the 3D power distribution in both principal planes at the operation frequency, corresponding to the results shown in Fig. 4(b,e).

5.   Experimental and numerical results of the power distribution at 0.675 THz

The experimental and numerical results of the power distribution on both xz and yz focal planes at $f = 0.675$ THz and $f = 0.692$ THz, respectively, were shown and discussed in Fig. 4. These frequencies were selected by extracting the maximum field distribution from the spectral response shown in Fig. 3(a,b). To further evaluate the response of the ENZ-GRIN lens, it is also interesting to evaluate its performance at the same frequency. For the sake of completeness, the numerical results of the power distribution on both xz and yz focal planes are shown in Fig. 9 at the frequency of maximum field from the experiment ($f = 0.675$). From these results we get FWHMx = 0.242 mm = 0.54λ and FWHMy = 0.31 mm = 0.7λ

which are in agreement with the experimental results obtained from Fig. 4(a,d) with values of FWHMx

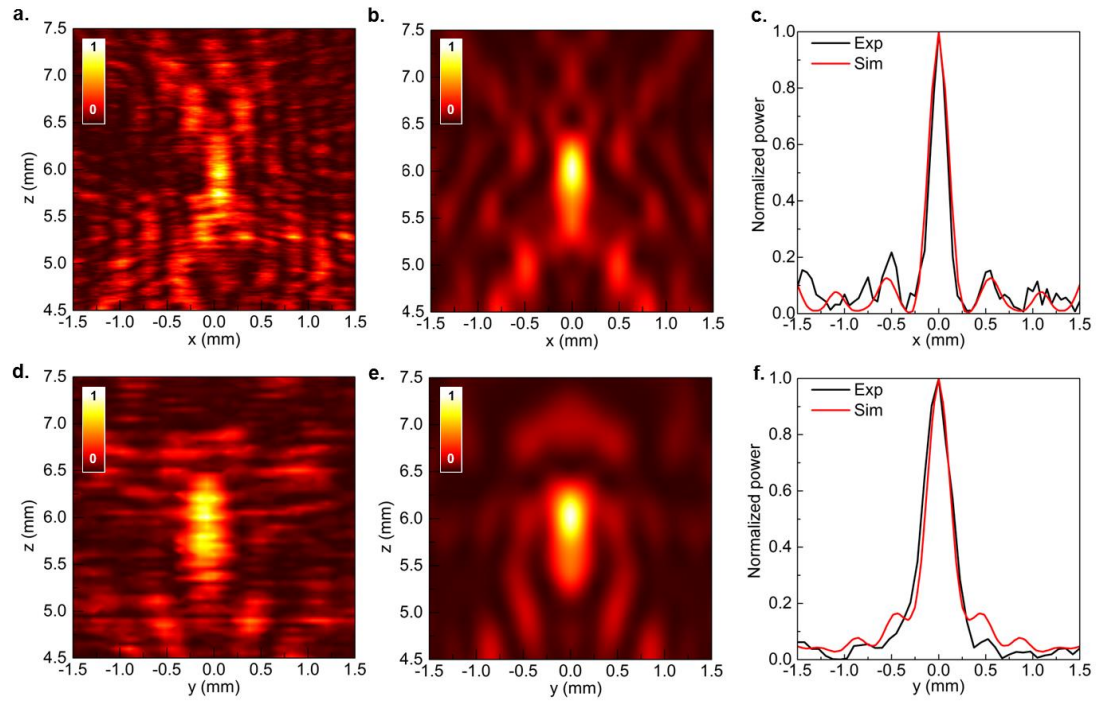= 0.217 ± 0.1 mm = (0.488λ ± 0.025)λ and FWHMy = 0.337 ± 0.1 mm = (0.76λ ± 0.025)λ.

Figure. 9. Experimental and numerical results of the power distribution on the focal planes at 0.675 THz: (a,d) experimental results on the *xz* and *yz* planes, respectively, (b,e) numerical results on the *xz* and *yz* planes, respectively. (c,f) experimental (black lines) and numerical (red lines) results of the power distribution at the focal position along the *x* and *y* axes, respectively.

REFERENCES

(1) Veselago, V. G. The Electrodynamics of Substances with Simultaneously Negative Values of ε and μ. *Sov. Phys. Uspekhi* **1968**, *10*, 509–514.

(2) Parazzoli, C. G.; Greegor, R. B.; Nielsen, J. A.; Thompson, M. A.; Li, K.; Vetter, A. M.; Tanielian, M. H.; Vier, D. C. Performance of a Negative Index of Refraction Lens. *Appl. Phys. Lett.* **2004**, *84*, 3232–3234.

(3) Shelby, R. A.; Smith, D. R.; Schultz, S. Experimental Verification of a Negative Index of Refraction. *Science* **2001**, *292*, 77–79.

(4) Dolling, G.; Enkrich, C.; Wegener, M.; Soukoulis, C. M.; Linden, S. Simultaneous Negative Phase and Group Velocity of Light in a Metamaterial. *Science* **2006**, *312*, 892–894.

(5) Liu, H.; Lalanne, P. Microscopic Theory of the Extraordinary Optical Transmission. *Nature* **2008**, *452*, 728–731.

(6) Solymar, L.; Shamonina, E. *Waves in Metamaterials*; Oxford University Press: New York, 2009.

(7) Vesseur, E. J. R.; Coenen, T.; Caglayan, H.; Engheta, N.; Polman, A. Experimental Verification of n=0 Structures for Visible Light. *Phys. Rev. Lett.* **2013**, *110*, 13902.

(8) Moitra, P.; Yang, Y.; Anderson, Z.; Kravchenko, I. I.; Briggs, D. P.; Valentine, J. Realization of an All-Dielectric Zero-Index Optical Metamaterial. *Nat. Photonics* **2013**, *7*, 1–5.

(9) Della Giovampaola, C.; Engheta, N. Digital Metamaterials. *Nat. Mater.* **2014**, *13*, 1115–1121.

(10) Zhou, F.; Cao, W.; Dong, B.; Reissman, T.; Zhang, W.; Sun, C. Additive Manufacturing of a 3D Terahertz Gradient-Refractive Index Lens. *Adv. Opt. Mater.* **2016**.

(11) Li, Y.; Liberal, I.; Giovampaola, C. Della; Engheta, N. Waveguide Metatronics : Lumped Circuitry Based on Structural Dispersion. *Sci. Adv.* **2016**, *2*, 1–8.

(12) Silva, A.; Monticone, F.; Castaldi, G.; Galdi, V.; Alù, A.; Engheta, N. Performing Mathematical Operations with Metamaterials. *Science (80-.).* **2014**, *343*, 160–163.

(13) Zheludev, N. I.; Kivshar, Y. S. From Metamaterials to Metadevices. *Nat. Mater.* **2012**, *11*, 917–924.

(14) Maas, R.; van de Groep, J.; Polman, A. Planar Metal/dielectric Single-Periodic Multilayer Ultraviolet Flat Lens. *Optica* **2016**, *3*, 592.

(15) Silveirinha, M.; Engheta, N. Tunneling of Electromagnetic Energy through Subwavelength Channels and Bends Using ε-Near-Zero Materials. *Phys. Rev. Lett.* **2006**, *97*, 157403-1–4.

(16) Silveirinha, M.; Engheta, N. Theory of Supercoupling, Squeezing Wave Energy, and Field Confinement in Narrow Channels and Tight Bends Using ε near-Zero Metamaterials. *Phys. Rev. B* **2007**, *76*, 245109.

(17) Engheta, N. Circuits with Light at Nanoscales: Optical Nanocircuits Inspired by Metamaterials. *Science* **2007**, *317*, 1698–1702.

(18) Alù, A.; G. Silveririnha, M.; Engheta, N. Transmission-Line Analysis of ε-near-Zero – Filled Narrow Channels. *Phys. Rev. E* **2008**, *78*, 16604-1–10.

(19) Pollard, R. J.; Murphy, A.; Hendren, W. R.; Evans, P. R.; Atkinson, R.; Wurtz, G. A.; Zayats, A. V.; Podolskiy, V. A. Optical Nonlocalities and Additional Waves in Epsilon-near-Zero Metamaterials. *Phys. Rev. Lett.* **2009**, *102*, 1–4.

(20) Maas, R.; Parsons, J.; Engheta, N.; Polman, A. Experimental Realization of an Epsilon-near-Zero Metamaterial at Visible Wavelengths. *Nat. Photonics* **2013**, *7*, 907–912.

(21) Yang, X.; Hu, C.; Deng, H.; Rosenmann, D.; David, A.; Gao, J. Experimental Demonstration of near-Infrared Epsilon-near-Zero Multilayer Metamaterial Slabs. *Opt. Express* **2013**, *21*, 23631–23639.

(22) Rodríguez-Fortuño, F. J.; Vakil, A.; Engheta, N. Electric Levitation Using ε-Near-Zero Metamaterials. *Phys. Rev. Lett.* **2014**, *112*, 33902.

(23) Kinsey, N.; DeVault, C.; Kim, J.; Ferrera, M.; Shalaev, V. M.; Boltasseva, A. Epsilon-near-Zero Al-Doped ZnO for Ultrafast Switching at Telecom Wavelengths. *Optica* **2015**, *2*, 616–622.

(24) Rizza, C.; Di Falco, A.; Scalora, M.; Ciattoni, A. One-Dimensional Chirality: Strong Optical Activity in Epsilon-Near-Zero Metamaterials. *Phys. Rev. Lett.* **2015**, *115*, 1–5.

(25)   Engheta, N. Pursuing Near-Zero Response. *Science (80-.).* **2013**, *340*, 286–287.

(26)   Edwards, B.; Alù, A.; Young, M. E.; Silveirinha, M.; Engheta, N. Experimental Verification of Epsilon-near-Zero Metamaterial Coupling and Energy Squeezing Using a Microwave Waveguide. *Phys. Rev. Lett.* **2008**, *100*, 1–4.

(27)   Ciattoni, A.; Rizza, C.; Marini, A.; Di Falco, A.; Faccio, D.; Scalora, M. Enhanced Nonlinear Effects in Pulse Propagation through Epsilon-near-Zero Media. *Laser Photonics Rev.* **2016**, *10*, 517–525.

(28)   Pacheco-Peña, V.; Navarro-Cía, M.; Beruete, M. Epsilon-near-Zero Metalenses Operating in the Visible. *Opt. Laser Technol.* **2016**, *80*, 162–168.

(29)   Ciattoni, A.; Marini, A.; Rizza, C. Efficient Vortex Generation in Subwavelength Epsilon-Near-Zero Slabs. *Phys. Rev. Lett.* **2017**, *118*, 1–5.

(30)   Alù, A.; Engheta, N. Dielectric Sensing in ϵ-near-Zero Narrow Waveguide Channels. *Phys. Rev. B* **2008**, *78*, 45102.

(31)   Powell, D.; Alù, A.; Edwards, B.; Vakil, A.; Kivshar, Y.; Engheta, N. Nonlinear Control of Tunneling through an Epsilon-near-Zero Channel. *Phys. Rev. B* **2009**, *79*, 245135.

(32)   Alù, A.; Silveirinha, M.; Salandrino, A.; Engheta, N. Epsilon-near-Zero Metamaterials and Electromagnetic Sources: Tailoring the Radiation Phase Pattern. *Phys. Rev. B* **2007**, *75*, 155410.

(33)   Navarro-Cía, M.; Beruete, M.; Sorolla, M.; Engheta, N. Lensing System and Fourier Transformation Using Epsilon-near-Zero Metamaterials. *Phys. Rev. B* **2012**, *86*, 165130-1–6.

(34)   Torres, V.; Pacheco-Peña, V.; Rodríguez-Ulibarri, P.; Navarro-Cía, M.; Beruete, M.; Sorolla, M.; Engheta, N. Terahertz Epsilon-near-Zero Graded-Index Lens. *Opt. Express* **2013**, *21*, 9156–9166.

(35)   Pacheco-Peña, V.; Torres, V.; Beruete, M.; Navarro-Cía, M.; Engheta, N. ϵ -near-Zero (ENZ) Graded Index Quasi-Optical Devices: Steering and Splitting Millimeter Waves. *J. Opt.* **2014**, *16*, 94009.

(36)   Torres, V.; Orazbayev, B.; Pacheco-Peña, V. V.; Teniente, J.; Beruete, M.; Navarro-Cia, M.; Sorolla, M.; Engheta, N.; Navarro-Cía, M.; Engheta, N. Experimental Demonstration of a Millimeter-Wave Metalic ENZ Lens Based on the Energy Squeezing Principle. *IEEE Trans. Antennas Propag.* **2015**, *63*, 231–239.

(37)   Alù, A.; Engheta, N. Boosting Molecular Fluorescence with a Plasmonic Nanolauncher. *Phys. Rev. Lett.* **2009**, *103*, 43902.

(38)   Alù, A.; Engheta, N. Coaxial-to-Waveguide Matching with ε-Near-Zero Ultranarrow Channels and Bends. *IEEE Trans. Antennas Propag.* **2010**, *58*, 328–339.

(39)   Gao, J.; Sun, L.; Deng, H.; Mathai, C. J.; Gangopadhyay, S.; Yang, X. Experimental Realization of Epsilon-near-Zero Metamaterial Slabs with Metal-Dielectric Multilayers. *Appl. Phys. Lett.* **2013**, *103*, 51111.

(40)   Siegel, P. H. Terahertz Technology. *IEEE Trans. Microw. Theory Tech.* **2002**, *50*, 910–928.

(41)   Ferguson, B.; Zhang, X.-C. Materials for Terahertz Science and Technology. *Nat. Mater.* **2002**, *1*, 26–33.

(42)   Chen, H. T.; Padilla, W. J.; Zide, J. M. O.; Gossard, A. C.; Taylor, A. J.; Averitt, R. D. Active Terahertz Metamaterial Devices. *Nature* **2006**, *444*, 597–600.

(43)   Chen, H.-T.; Padilla, W. J.; Cich, M. J.; Azad, A. K.; Averitt, R. D.; Taylor, A. J. A Metamaterial Solid-State Terahertz Phase Modulator. *Nat. Photonics* **2009**, *3*, 148–151.

(44)   Ho, L.; Pepper, M.; Taday, P. Terahertz Spectroscopy: Signatures and Fingerprints. *Nat. Photonics* **2008**, *2*, 541–543.

(45)   Rodríguez-Ulibarri, P.; Kuznetsov, S. A.; Beruete, M. Wide Angle Terahertz Sensing with a Cross-Dipole Frequency Selective Surface. *Appl. Phys. Lett.* **2016**, *108*.

(46)   Karl, N. J.; Mckinney, R. W.; Monnai, Y.; Mendis, R.; Mittleman, D. M. Frequency-Division Multiplexing in the Terahertz Range Using a Leaky-Wave Antenna. *Nat. Photonics* **2015**, *9*, 717–720.

(47)   Scherger, B.; Jördens, C.; Koch, M. Variable-Focus Terahertz Lens. *Opt. Express* **2011**, *19*, 4528.

(48)   Wang, X.; Xie, Z.; Sun, W.; Feng, S.; Cui, Y.; Ye, J.; Zhang, Y. Focusing and Imaging of a Virtual All-Optical Tunable Terahertz Fresnel Zone Plate. *Opt. Lett.* **2013**, *38*, 4731.

(49) Chen, H.-T.; O'Hara, J. F.; Azad, A. K.; Taylor, A. J.; Averitt, R. D.; Shrekenhamer, D. B.; Padilla, W. J. Experimental Demonstration of Frequency-Agile Terahertz Metamaterials. *Nat. Photonics* **2008**, *2*, 295–298.

(50) Lee, S. H.; Kim, H. D.; Choi, H. J.; Kang, B.; Cho, Y. R.; Min, B. Broadband Modulation of Terahertz Waves with Non-Resonant Graphene Meta-Devices. *IEEE Trans. Terahertz Sci. Technol.* **2013**, *3*, 764–771.

(51) Rizza, C.; Ciattoni, A.; Columbo, L.; Brambilla, M.; Prati, F. Terahertz Optically Tunable Dielectric Metamaterials without Microfabrication. *Opt. Lett.* **2013**, *38*, 1307.

(52) Rotman, W. Plasma Simulation by Artificial Dielectrics and Parallel-Plate Media. *IRE Trans. Antennas Propag.* **1962**, *10*, 82–95.

(53) Neu, J.; Beigang, R.; Rahm, M. Metamaterial-Based Gradient Index Beam Steerers for Terahertz Radiation. *Appl. Phys. Lett.* **2013**, *103*, 41109-1–4.

(54) Kock, W. E. Metal-Lens Antennas. *Proc. IRE* **1946**, *34*, 828–836.

(55) Hristov, H. D. *Fresnel Zones in Wireless Links, Zone Plate Lenses and Antennas*; Artech House: Inc., Norwood, MA, 2000.

(56) Mendis, R.; Nagai, M.; Wang, Y.; Karl, N.; Mittleman, D. M. Terahertz Artificial Dielectric Lens. *Sci. Rep.* **2016**, *6*, 1–8.

(57) Llombart, N.; Chattopadhyay, G.; Skalare, A.; Mehdi, I. Novel Terahertz Antenna Based on a Silicon Lens Fed by a Leaky Wave Enhanced Waveguide. *IEEE Trans. Antennas Propag.* **2011**, *59*, 2160–2168.

(58) Pfeiffer, C.; Grbic, A. Millimeter-Wave Transmitarrays for Wavefront and Polarization Control. *IEEE Trans. Microw. Theory Tech.* **2013**, *61*, 4407–4417.

(59) Monticone, F.; Estakhri, N. M.; Al??, A. Full Control of Nanoscale Optical Transmission with a Composite Metascreen. *Phys. Rev. Lett.* **2013**, *110*, 203903-1–5.

(60) Gentselev, A. N.; Goldenberg, B. G.; Kuznetsov, S. A. Microstructured Elements for Electromagnetic Radiation Selection and the Method for Their Fabrication. 2548945, 2015.

(61) Kuznetsov, S. A.; Et.al. High-Performance Subterahertz High-Pass Filters and Planar Focusing Structures Produced with Deep X-Ray Lithography (Submitted). *Appl. Phys. Lett.* **2016**.

(62) Saile, V.; Wallrabe, U.; Tabata, O.; Korvink, J. G. LIGA and Its Applications. In *Advanced micro & nanosystems*; Wiley-VCH, 2009.